ELECTROSPRAY POWER PROCESSING UNIT FOR A MONOPROPELLANT-ELECTROSPRAY MULTIMODE THRUSTER

BY

JACOB EISEN

THESIS

Submitted in partial fulfillment of the requirements
for the degree of Master of Science in Aerospace Engineering
in the Graduate College of the
University of Illinois Urbana-Champaign, 2022

Urbana, Illinois

Adviser:

Professor Joshua L. Rovey

ABSTRACT

Multimode space propulsion combines two or more propulsive methods into a single system with a shared propellant, the goal of which is to offer spacecraft improved maneuver flexibility and efficiency. A power processing unit (PPU) is described and developed here to meet the high-voltage low-power needs of the electrospray mode of a monopropellant-electrospray multimode thruster. The PPU is resilient to the variable-load nature of electrospray thrusters, producing a consistent output voltage regardless of the thruster's current draw. The PPU consists of a two-phase interleaved boost converter, transformer, and Cockcroft-Walton voltage multiplier. By designing a transformer magnetizing inductance of at least 1 mH and using a 10 MΩ bleed resistor at the PPU output, discontinuous conduction mode is avoided during the thruster startup period before Taylor cone formation. This allows the desired thruster voltage of 3.25 kV to be maintained both during and after thruster startup. A 20 MΩ current-limiting resistor placed just before the thruster prevents PPU component damage during thruster shorts. The presence of this resistor also maintains the voltage multiplier output voltage even if the thruster voltage itself cannot be sustained without overcurrent, allowing nominal electrospraying to resume if the thruster recovers from the short. The PPU is integrated with a real multimode thruster for a ground-based test to prove its suitability for the application, marking the first time a purpose-built electrospray PPU has been successfully applied to a monopropellant-electrospray multimode thruster.

ACKNOWLEDGEMENTS

My first thanks go to my adviser, Dr. Rovey, for giving me this opportunity and so much support. This would of course not have been possible without you, and you have shown me great patience and kindness throughout this graduate degree. I would also like to thank other members of the EPLab at University of Illinois Urbana-Champaign for their collaborations and help, in particular Chris Lyne, Bryan Cline, and Matthew Paliwoda. Work performed by Kartikeya Veeramraju and Dr. Jonathan Kimball from Missouri University of Science and Technology provided the foundation for this power processing unit, and they have given invaluable support throughout the project duration. Thomas Liu, Corey Rhodes, and Luis Pinero (NASA Glenn Research Center) and Khary Parker (NASA Goddard Space Flight Center) are greatly appreciated for the essential technical insight and project guidance they have supplied. This work was supported in part by NASA as part of the SmallSat Technology Partnerships program (grant number 80NSSC20M0089). Finally, I offer deep and sincere gratitude to my family at home and my friends and partner at UIUC. You have seen and shared in everything I have felt. Thank you for being who you are.

TABLE OF CONTENTS

CHAPTER 1: INTRODUCTION

Multimode space propulsion systems integrate two or more propulsive modes into a single system with shared propellant[1]. The commonality of propellant between modes differentiates this form of spacecraft propulsion from hybrid propulsion systems. Multimode propulsion systems offer increased mission design flexibility and can simplify the process of propulsion system selection. The choice between thrust modes can be leveraged to facilitate on-the-fly mission design, and it may increase the number of solutions available when responding to a change in spacecraft or environment status. As in-space missions continue to grow quickly in quantity and complexity[2], the one-size-fits-many nature of multimode space propulsion systems may make them appealing as a generalized thrust solution.

One type of multimode system is the monopropellant-electrospray combination. While in monopropellant (chemical decomposition) mode, these multimode systems operate at a relatively high thrust and relatively low specific impulse; when in electrospray mode, they operate at a *lower* thrust and *higher* specific impulse[1]. After assessing various combinations of chemical-electric multimode propulsion, Rovey et al. found that monopropellant-electrospray multimode systems cover a significantly larger mission design trade space than when the constituent propulsion systems are used separately[3]. This means that these thrust options are useful across a wide range of missions. For example, satellites operating in low Earth orbit often require efficient low-thrust propulsion systems for station-keeping. As this environment becomes increasingly crowded with small satellites, a higher-thrust option can also be useful for faster orbit modification when one satellite is predicted to collide with another. In this way, multimode propulsion systems can improve satellite safety and reliability as part of a contingency plan. Falcone et al. found that for satellite servicing applications such as orbit maintenance and propellant refilling, multimode monopropellant-electrospray propulsion systems offer greater servicing mission flexibility than existing electric and chemical propulsion systems with a lower propulsion system dry mass than existing hybrid systems[4]. Rexius and Holmes investigated time-sensitive plane-change maneuvers (which may be necessary for such satellite servicing missions) and found that multimode systems may allow for propellant savings when performing these maneuvers[5]. Long-duration interplanetary missions are an additional class of applications which might make effective use of multimode propulsion systems. These missions may require a low-thrust mode for course correction and a high-thrust mode for orbit insertion at the destination body. After insertion, the spacecraft's orbit may need to be modified or maintained, either of which can be achieved using the low-thrust high-ISP mode. Cline et al. developed an analytical method for interplanetary mission propulsion selection; they found that for multimode systems

which include high-performing chemical and electric propulsion systems, some Earth-Mars missions benefit from multimode systems due to increased transfer rates (over missions attempting to use purely chemical or purely electric propulsion)[6]. This variety of applications has inspired more granular development of the sub-systems involved in multimode propulsion.

One such sub-system is the power processing unit (PPU), which converts power from the spacecraft bus to control the voltage and current delivered to a thruster in order to meet its operating requirements. Depending on the thruster, the PPU may meet demands beyond thruster power, such as thruster status monitoring, thruster control systems, communications, and propellant delivery. Monopropellant-electrospray multimode systems have different demands of the on-board PPU depending on the mode in which they are operating.

A. ELECTROSPRAY THRUSTERS AND THEIR CHALLENGES FOR A PPU

Electrospray thrusters use a high voltage generated by the PPU to eject ions and charged droplets into space. These thrusters contain one or more emitters and an extractor grid. Three main types of emitters exist: capillary, porous, and externally-wetted. The emitters and the extractor grid are carefully aligned at a close distance to one another, and a high voltage is placed across the two. For electrospray thrusters which use capillary-type emitters, this high voltage serves to draw ionic liquid through the emitter channels and form Taylor cones at the exit of each emitter. At the tip of a Taylor cone exists an extremely high-magnitude electric field, the presence of which causes high-velocity emission of ions and charged droplets. These pass through gaps in the extractor grid and are ejected into space. The applied voltage may range from a few hundred volts to several kV, with the ion and droplet emission resulting in low currents up to several hundred µA[7–13].

The electrospray PPU discussed in this paper specifically targets the Monopropellant-Electrospray Propulsion System (MEPS), developed via a collaboration between The Electric Propulsion Laboratory (EPLab) at University of Illinois Urbana-Champaign and Froberg Aerospace LLC. MEPS is a multimode system which uses a single thruster in both monopropellant and electrospray modes. The associated thruster hardware is the culmination of a great deal of research on thrust methods suitable for combination, as well as applications and conditions under which its effectiveness is maximized[1]. Establishing an appropriate propellant is one of the greatest challenges for multimode propulsion, as the propellant must function within the thrust method of all modes. The MEPS thruster was designed for use with FAM-110A propellant (Froberg Aerospace Multimode Propellant 110A), a novel ionic liquid composed of a 41%–59% (by weight) mixture of $Emim - EtSO_4$ and HAN[14–16]. FAM-110A has been used successfully during MEPS thruster tests in both chemical decomposition mode and electrospray mode[17, 18].

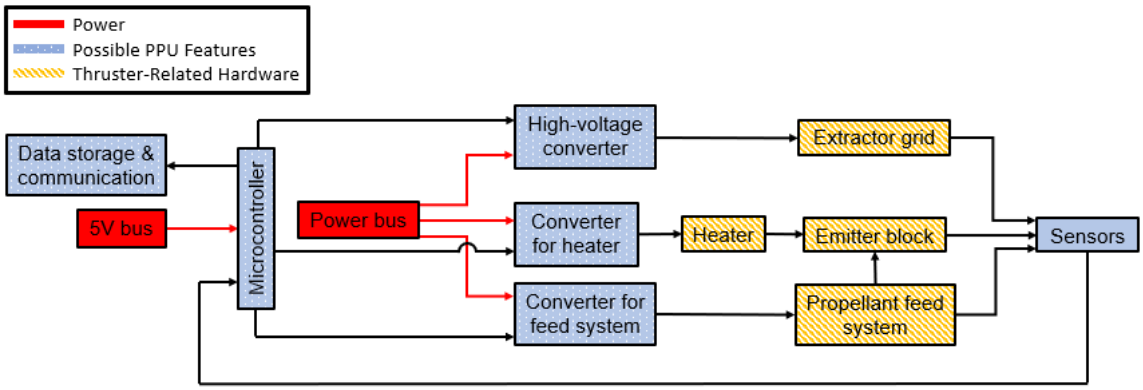

Fig. 1 Block Diagram for Notional Full PPU System

The thruster itself is a stainless steel block, one face of which exhibits a 16 by 16 array of parallel capillary-type emitters (for 256 emitters in total). Each channel's interior walls are coated in a layer of platinum catalyst that assists with propellant decomposition when the thruster is used in chemical mode. The high-temperature products are subsequently exhausted from the emitter tips, generating thrust. Again, in electrospray mode, thrust is generated via the ejection of propellant ions and droplets which are pulled from the emitter tips using a high emitter-extractor voltage.

Fig. 1 is a block diagram of a notional PPU system, showing how it might interface with the MEPS thruster on-board a spacecraft. As previously stated, a full PPU system would likely perform tasks beyond power conversion (such as communications and propellant delivery control, as shown in the diagram). However, this paper's primary focus is the development of the high-voltage converter block shown in the diagram, used to generate the high voltage for electrospray operation. This high-voltage converter (along with the microcontroller and associated power) is referred to as the "PPU" throughout this paper.

There are several critical considerations when designing a PPU to provide the high voltage for electrospray thruster operation. For one, this high voltage must be carefully maintained within certain limits. The voltage's lower bound is determined by the thruster's minimum emission voltage (i.e., its turn-on voltage). Allowing the thruster voltage to fall below this level during spray can cause Taylor cone collapse and flooding of the emitter channel array. Running an electrospray thruster at too high a voltage can strip the Taylor cones of liquid at an untenable rate, similarly causing their collapse and subsequent thruster flooding.

Additionally, this high voltage may need to alternate for at least two reasons. The first is that thruster operation at a single voltage polarity may cause spacecraft charging, as only ions of one polarity are being ejected from the spacecraft into space[19]. The second is that maintaining single-polarity operation for an

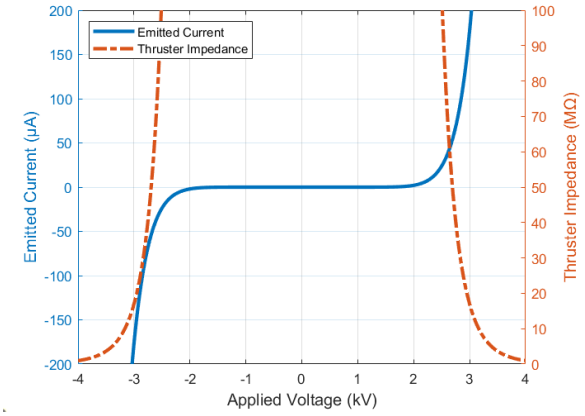

Fig. 2 IV Curve Example

extended period of time may change the propellant's physical and chemical properties[20]. This requirement was not deemed critical for this ground-based iteration of the PPU, but a PPU which *allows* for dual-polarity operation is preferable.

In capillary-type electrospray thrusters such as the one built for MEPS, the ionic liquid contained by the emitters has an intrinsic electrical connection to the propellant tank and feed system which surrounds it (unless their insides are coated). If the tank and feed system are connected directly to the satellite chassis in a real spaceflight application, the emitters must remain at ground rather than having a potential applied to them. Therefore, a PPU which allows the emitters to remain grounded is preferred. Mier-Hicks and Lozano showed that a floating ground on a PPU's high-voltage side can aid satellite charge neutralization if two electrospray thrusters are operating simultaneously at opposite polarities[19]. The usefulness of a floating high-voltage ground should therefore not be discounted, but possible difficulties associated with the practical implementation of such isolation on a satellite makes preferable a PPU design which allows for grounded emitters.

Electrospray thrusters can be characterized using an IV (current-voltage) curve. An example of an IV curve is shown in Fig. 2 (this figure does not represent actual MEPS data; it is just for demonstration's sake). The purpose of generating this curve is to determine the relationship between the applied voltage and the emitted current for that particular thruster. As this relationship is nonlinear, it is clear that the thruster's effective electrical resistance changes as a function of the emitter-extractor voltage. For the PPU designer, this means electrospray thrusters cannot be characterized as an electrical load with a single and unchanging resistance. Additionally, their current draw varies dramatically over the course of their operation even while the applied voltage remains fixed. During thruster startup, the propellant takes time to reach the emitter tips

and form Taylor cones. The thruster therefore draws nearly no current during startup, giving it an effectively infinite electrical resistance (a no-load condition). Once propellant begins to reach the emitter tips, emitters may turn "on" in a staggered fashion due to slight differences in their geometry. Even once all emitters are spraying, intermittent (or long-term) emitter-extractor shorts are a possibility, during which the thruster's electrical resistance drops significantly. The ST7-DRS payload on-board the LISA Pathfinder spacecraft suffered what was likely an emitter-extractor short in one of its electrospray thrusters, effectively ending the thruster's intended function[13]. Both intermittent and spray-ending shorts have been observed in the iEPS (ion electrospray propulsion system) developed at MIT's Space Propulsion Laboratory[21]. As discussed in [18, 22, 23], these thruster shorts may be the product of effects such as propellant backspray from the extractor, emitter flooding as a result of propellant wicking, or sudden bursts of propellant from the emitter tips due to impurities in the ionic liquid. These electrospray thruster characteristics all lead to a widely-varying electrical resistance that demands a resilient and reliable PPU.

B. ELECTROSPRAY PPU APPROACHES

Some electrospray PPUs use commercial high-voltage converters, a sensible solution for projects aiming to achieve rapid ground-based thruster testing. For example, the converters built in [21, 24, 25] all use A Series high-voltage DC-DC converters from XP Power/EMCO, compact components capable of producing both positive and negative high voltage at up to 1 W. However, no off-the-shelf high-voltage DC-DC converters exist at present which are rad-hard or rated for in-space application. For projects aiming at eventual in-space use, commercial converters are unfortunately a temporary solution for ground-based testing at present. EPLab therefore opted to begin the process of designing, building, and testing a custom PPU at this point to avoid rushed development in the future.

Several different custom PPU topologies have been designed to overcome the challenges unique to electrospray thruster operation. By itself, generating several kilovolts is achievable through a wide variety of converters making use of options including boost-derived topologies, bridge converters, transformers, multilevel converters, and voltage multipliers[26–28]. Cockcroft-Walton voltage multipliers (CWVMs) in particular are a common feature of electrospray PPUs since they provide a voltage increase *and* serve as a rectifier[25, 29–34]. Hansel investigated the effectiveness of staging a modified flyback converter and a voltage multiplier for use with a scaled-down version of MIT's iEPS[33]. The topology's planar (coreless) magnetics allowed its miniaturization and could also be used as an antenna for communication with other small satellites. However, the modified flyback converter does not provide for isolation between the high-voltage

and low-voltage sides of the converter, which is preferred both for the safety of humans and any components on the converter's low-voltage side. The converter developed by Visee at al. uses a topology based on the Royer oscillator to generate a high-voltage AC signal, feeding it to a CWVM to generate up to 3.8 kV[34]. This topology does not allow for emitter grounding however, as the emitter-extractor voltage difference is modified via the use of a controllable resistive voltage divider which feeds a reduced version of the same high voltage to the other electrode (creating a voltage difference between the two). Stelwagen et al. also built a converter using a Royer oscillator, controlling its output voltage via a feedback system that enabled accuracy within 3 V[35]. Veeramraju and Kimball use a two-phase interleaved boost converter (TPIBC) to feed an AC signal to a transformer, with rectification and further boosting performed by CWVMs[31]. This topology is an updated version of the PPU designed by Baddipadiga et al. which had used coupled inductors rather than a transformer[30, 36]. Replacing the coupled inductors with a transformer reduced output voltage ripple and solved a practical grounding issue. This newer topology—a TPIBC, transformer, and CWVMs—was chosen as the foundation for the MEPS electrospray PPU. It allows for dual-mode operation and emitter grounding, also offering isolation and voltage controllability. The benefits of this topology are explored in more detail in Chapter 2.A.i. As the topology is the product of several iterations and is explored in-detail in literature, its working mechanisms and benefits for the application were very clear.

An existing electrospray PPU topology[31] has been modified for use with the MEPS thruster. The PPU reaches the MEPS thruster's operating voltage using a combination of three voltage-boosting stages. In order, they are: a two-phase interleaved boost converter, a high-frequency transformer, and a Cockcroft-Walton voltage multiplier. It has a modifiable output voltage which is designed to remain stable even during thruster startup and thruster shorts. After simulations and standalone hardware tests which proved the PPU suitable for this application, it was integrated with the MEPS thruster for a demonstration in electrospray mode. This demonstration is a first for the topology, as it had not previously been tested for compatibility with an actual electrospray thruster. This work represents the first custom-built power processing unit tested with a monopropellant-electrospray multimode thruster operating in electrospray mode.

CHAPTER 2: PPU DESIGN AND SIMULATION

A. ANALYTICAL DESIGN

i. TOPOLOGY OVERVIEW

First and foremost, it is useful to step through the fundamentals of this topology. A boost converter functions to increase voltage and is traditionally considered a DC-DC circuit. The DC output of a boost converter contains a ripple characteristic defined by the converter's output capacitance. Boost converters can be interleaved in order to reduce this ripple and improve efficiency. The interleaving in this topology serves a different purpose, however. Within the electrospray PPU TPIBC, each boost converter takes turns firing. Rather than rectifying these signals and feeding both to the same side of a load (as in a conventional interleaved boost converter), each boost inductor output is fed to opposite ends of a single transformer primary. The boost inductors operate perfectly out-of-phase to generate what is effectively an AC signal for the transformer. This signal takes the shape of a modified square wave (MSW). The transformer then boosts this MSW, with the secondary connected to the CWVMs. The CWVMs provide further boosting and rectification. A circuit diagram for this topology is shown in Fig. 3.

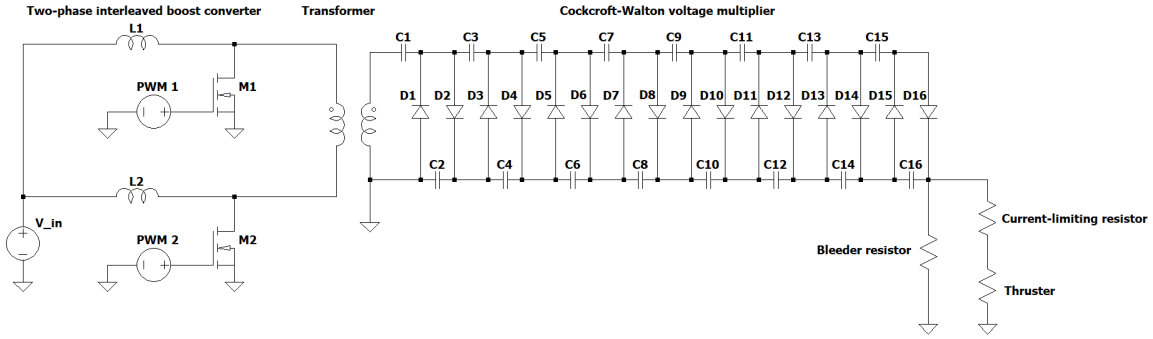

Fig. 3 Electrospray PPU Circuit Diagram

This converter topology offers a number of features that are beneficial to electrospray application. The voltage delivered by a boost converter can be changed by altering the duty cycle of the MOSFET switching signals. This means that the electrospray PPU final output voltage is modifiable, and power cycling the PPU is unnecessary when making these dynamic adjustments. The feature allows for closed-loop control of the PPU output voltage (previously accomplished with this topology in [29]). Additionally, the transformer separates the high-voltage and low-voltage sides of the PPU, providing electrical isolation between them. In the event of a PPU fault, this isolation can help protect the TPIBC as well as any measurement devices or other

Table 1 MEPS Thruster Nominal Electrical Characteristics, in Electrospray Mode

Emitters Active	Voltage (V)	Current (μA)	Resistance (MΩ)	Power (W)
6 Emitters	3250	9.5	350	0.0308
Full Array (256)	3250	404.5	8.03	1.31

peripherals operating on the PPU's low-voltage side. CWVMs are a form of staged capacitor-diode multipliers in which the output voltage is distributed equally across each stage, rather than being impressed across a single output capacitor. This feature allows for high output voltages with lower voltage ratings for each individual component. The risks of arcing and/or dielectric degradation are reduced as a result, due to the simultaneous decrease in component voltage ratings and increase in distance between the high-voltage output terminals. This is particularly impactful in the context of in-space applications where form factor is key. Though the PPU discussed here is designed with only one CWVM in mind, it is possible to add a second CWVM in parallel with the first (as in [31]) for the purpose of generating an opposite-polarity high voltage. A high-voltage switch can then be used to alternate which CWVM is attached to the thruster.

ii. AVAILABLE POWER AND PPU LOADING

The MEPS thruster has previously been operated in electrospray mode with an emitter-extractor voltage of 3.25 kV DC [18]. This preliminary test drew up to 9.5 μA with 6 emitters active during nominal spraying, which gives an estimate for per-emitter current of up to 1580 nA. During a 6-emitter test, the nominal thruster resistance is therefore approximately 350 MΩ. By multiplying together the emitter-extractor voltage and the nominal thruster current for 6-emitter spray, it can be seen that the electrospray PPU demands approximately 31 mW. The PPU is designed to work with this set of nominal MEPS thruster conditions.

As an addendum, the total current produced by the entire 256-emitter array is estimated to be 404.5 μA by using the previously calculated per-emitter current. The thruster's resistance during full-array nominal spray is therefore estimated at 8.03 MΩ, and the thruster power estimated at 1.31 W. Though this specific PPU is not designed with this set of nominal conditions in mind, the same overarching topology may still be used.

The PPU input voltage must be determined. LiPo batteries and 18650 Li-ion batteries have both been used in many small satellite applications [37–40]. LiPo batteries which provide 7.4 V DC are commercially available, and stacking two 18650 batteries also provides 7.4 V DC. This is a reasonable choice for a PPU input voltage as it is comfortably above the 5 V required for many electronics, yet not so high that space is wasted by stacking additional cells. The choice of input voltage is not strongly constrained, however, and a PPU designer might choose differently depending on the results of a tradeoff analysis or the requirements of

some other system.

At the CWVM output are two resistors. One is in parallel with the thruster—this bleeder resistor sets the minimum possible current draw from the CWVM. This consideration is essential, as this topology may experience a unique DCM if its power delivery is too low[41]. This results in the generation of higher-than-intended voltages at the CWVM output and could possibly lead to PPU or thruster damage. Recall that Table 1 shows a nominal power draw of only 31 mW during 6-emitter spray, making this DCM a concern. Additionally, since the MEPS thruster draws very little current during electrospray startup, this is an unavoidable condition under which the PPU must still operate nominally. The value of this bleeder resistor R_{bleed} is chosen to be 10 MΩ, to ensure there is always at least 1 W of power delivered at the CWVM output. This value can be tweaked throughout the design process as long as its effects on the design are properly accounted for (such as component ratings and duty cycle selection). 1 W was selected as a target for the minimum output power simply due to its proximity to the nominal output power for full-array operation, as full-array MEPS thruster spraying is the ultimate intended application for this PPU topology.

The other resistor is in series with (before) the thruster. This serves as a current-limiting resistor, since the thruster's electrical resistance drops dramatically during shorts. There are several considerations to make when sizing this resistor; firstly, it must not have a voltage drop across it such that the thruster voltage is significantly reduced during nominal operation. Secondly, it must appropriately limit the CWVM power output to protect PPU components from overcurrent. After choosing the allowable thruster voltage drop (during nominal spray) to be roughly 5%, the resistor size R_{lim} can be calculated as:

$$0.05 = \frac{R_{lim}}{R_{lim} + R_{thrust}} \tag{1}$$

where R_{thrust} is the electrical resistance of the thruster. For 6-emitter MEPS tests, Eq. (1) sets R_{lim} at about 18 MΩ. A resistor of this size would be subjected to only 1.5 mW, and would limit the CWVM output power to about 1.8W. The current-limiting resistor is therefore chosen to be a convenient 20 MΩ, which limits the power drawn at the CWVM output to 1.76 W and is predicted to cause a 5.5% drop in thruster voltage during 6-emitter nominal spray. With the assumption that a 7.4 V power supply will be used at the PPU input, the required gain of an electrospray PPU DC-DC topology is therefore $1.055(3250/7.4) \approx 464$. This increases the targeted CWVM output voltage to approximately 3.43 kV, in order to ensure that the thruster still receives 3.25 kV.

For full-array thruster tests, the resistance value R_{lim} would definitely need re-evaluation as the voltage drop

across the approximately 8.03 MΩ MEPS thruster would be greatly reduced by the presence of a 20 MΩ series resistor. Since decreasing R_{lim} would endanger the PPU components (unless they are swapped with components that have a higher current rating), R_{lim} would likely need to exist alongside additional current-limiting methods.

iii. BOOST CONVERTER DESIGN

The boost converter switching frequency can be selected; this is the frequency at which pulse-width modulation (PWM) signals will be supplied to the TPIBC MOSFET gates. Boost converters often operate in the range of several hundred kilohertz[42], though advancements in wide bandgap semiconductor materials have allowed for DC-DC converter switching frequencies of up to several MHz[43, 44]. The TPIBC switching frequency is chosen to be 100 kHz, mirroring the work done in [31]. Though this choice is on the lower end of the typical switching frequency range, its practical advantage is reducing the likelihood of parasitics-related problems in the high-frequency transformer[45]. This choice for switching frequency is not tightly constrained, and it is not optimized for tradeoffs between converter efficiency and size.

The TPIBC transfer function is given by

$$\frac{V_{out}}{V_{in}} = \frac{1}{1-d} \tag{2}$$

where d is the duty cycle of the PWM signals sent to the MOSFET gates, and V_{in} and V_{out} are the input and output voltages respectively. This is the same transfer function exhibited by traditional DC-DC boost converters; the only difference is that here, for the TPIBC, V_{out} more specifically refers to the amplitude of the AC signal produced at the TPIBC output.

A nominal TPIBC duty cycle must be selected with an adequate adjustment range. It can be initially established that the duty cycle has a hard lower bound of 50% as the selected PPU topology does not function as intended for duty cycles below this value. A duty cycle lower than 50% would create periods of time where neither TPIBC MOSFET is conducting, which would leave both boost inductors without a path to ground. This scenario would lead to unwanted flyback voltage spikes with the potential of component damage. As in [31], an effective minimum duty cycle of 55% was selected to create a buffer away from this undesired mode.

The nominal duty cycle can be chosen by first considering the significance of the minimum achievable thruster voltage. The MEPS electrospray tests performed in [18] include some using Emi-Im propellant, which has a lower operating voltage than the 3.25 kV used for FAM-110A propellant. The Emi-Im propellant was sprayed at 2125 V, and separate tests indicated a turn-on voltage of 2.3 kV. The ability to reach a thruster voltage as low as 2125 V is appealing since it means the PPU may be compatible with Emi-Im use as well.

Since this minimum thruster voltage will be produced at a TPIBC duty cycle of 55%, the necessary post-TPIBC gain can be approximately calculated as follows:

$$G_{fixed} = 2125 \frac{R_{lim} + R_{thrust}}{R_{thrust}} \frac{1 - d_{min}}{V_{in}} \tag{3}$$

where G_{fixed} is the fixed post-TPIBC gain (the product of the transformer and CWVM gains), R_{lim} is the resistance of the current-limiting resistor, R_{thrust} is the approximated nominal thruster resistance, d_{min} is the minimum allowed TPIBC duty cycle, and V_{in} is the PPU input voltage.

This calculation gives $G_{fixed} = 137$. Once G_{fixed} is determined, the nominal duty cycle d_{nom} can be approximated by:

$$\frac{V_{in}}{1 - d_{nom}} = \frac{3250}{G_{fixed}} \frac{R_{lim} + R_{thrust}}{R_{thrust}} \tag{4}$$

which results in a nominal duty cycle of approximately 70.6%.

The maximum duty cycle is limited by boost inductor copper loss, which affects both the converter gain and the efficiency as duty cycle increases [42]. Taking this effect into consideration, a modified equation showing the actual gain of a boost converter is written as:

$$\frac{V_{out}}{V_{in}} = \frac{1}{1 - d} \frac{1}{1 + \frac{R_L}{(1-d)^2 R_{load_{eff}}}} \tag{5}$$

where R_L is boost inductor resistance and $R_{load_{eff}}$ is the resistance across the TPIBC outputs.

For this topology, $R_{load_{eff}}$ is defined as

$$R_{load_{eff}} = (\frac{1}{G_{fixed}})^2 R_{load} \tag{6}$$

where R_{load} is the actual load resistance at the PPU's output and G_{fixed} refers to all voltage gain occurring after the TPIBC. In this topology, G_{fixed} is the combined gain of the transformer and a single CWVM, which was previously found to be 137. During nominal spray, R_{load} is simply $1/(\frac{1}{R_{bleed}} + \frac{1}{R_{thrust}+R_{lim}})$, which gives 9.74 MΩ. Therefore, according to Eq. (6), the resistance across the TPIBC outputs is 519 Ω during nominal spray.

Assuming a boost inductor series resistance on the order of 1 Ω, Eq. (5) therefore exhibits a peak at about $d = 0.95$, after which the gain begins to drop with increasing duty cycle. This puts a constraint on the TPIBC

maximum duty cycle.

The maximum duty cycle is also constrained by the effect of boost inductor series resistance on efficiency. From [42], the TPIBC efficiency can be written as:

$$\eta_{boost} = \frac{1}{1 + \frac{R_L}{(1-d)^2 R_{load_{eff}}}} \tag{7}$$

Given the resistance across the TPIBC outputs found earlier (519 Ω) and an inductor series resistance of 1 Ω, the TPIBC efficiency follows the curve shown in Fig. 4:

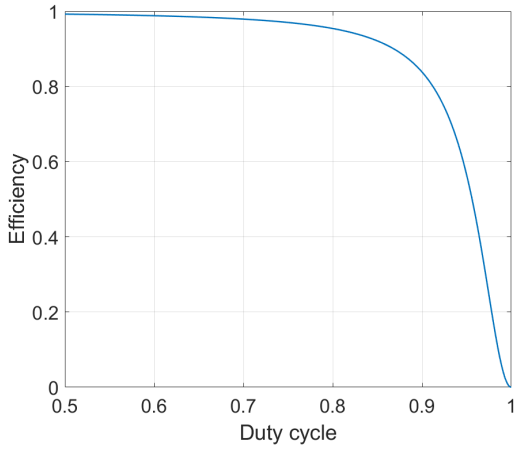

Fig. 4 Efficiency Model for Two-Phase Interleaved Boost Converter

Selecting a minimum TPIBC efficiency of 90% constrains the maximum duty cycle to 87%, which is lower maximum than the previously-established constraint of 95%.

Through this process, the nominal duty cycle was established to be 70.6%, adjustable down to 55% and as high as 87%. This results in a thruster voltage adjustable between (approximately) 2.12 kV and 7.32 kV, component voltage ratings notwithstanding.

The TPIBC boost inductors must have an inductance high enough to avoid discontinuous conduction mode (DCM). Reference [42] shows that minimum inductance to be governed by

$$L_{crit} \geq \frac{d_{min}(1 - d_{min})^2 R_{load_{eff}}}{2f} \tag{8}$$

where d_{min} is the minimum duty cycle of the signals driving the TPIBC, f is the frequency of those signals, and $R_{load_{eff}}$ is the load impedance across the TPIBC outputs. For the minimum duty cycle of 0.55, the operating frequency of 100 kHz, and the $R_{load_{eff}}$ previously calculated (519 Ω), $L_{crit} \geq 289$ µH. 800 mH

inductors were chosen for the boost inductance L_{boost}, to be well above this minimum.

During the TPIBC design, the post-TPIBC gain G_{fixed} (the gain from the transformer and CWVM combined) was fixed at 137. What remains is to distribute this gain between the transformer and CWVM. The transformer has some unique design constraints within this topology, and will therefore be discussed first.

iv. TRANSFORMER DESIGN

The high frequency transformer sits at the center of the electrospray PPU. The findings in [41] proved the transformer magnetization inductance to be a parameter of critical importance for low-power converters like this electrospray PPU. During MEPS electrospray mode startup, the propellant has not yet formed Taylor cones at the emitter tips, meaning the thruster draws far less current than during nominal spray. If the transformer magnetization inductance is too low (for a given TPIBC boost inductance and switching frequency), the boost inductor currents may not be sufficient to surpass the transformer magnetization current. This causes the converter to leave continuous conduction mode (CCM) which may create voltages at the CWVM output that are higher than those expected within CCM operation. These high (and load-dependent) voltages are unwanted in the context of MEPS thruster application, and may result in PPU component or thruster damage.

However, an unnecessarily large magnetization inductance has negative consequences as well. Reference [46] demonstrates a method of calculating magnetization inductance, using Eq. (9):

$$L_m = \frac{N_1^2}{\mathcal{R}} \tag{9}$$

Here, N_1 is the number of primary turns and $\mathcal{R}$ is the total core reluctance. From this relationship, it becomes clear that increasing magnetization inductance requires either increasing the primary turn count or reducing the total core reluctance, which would necessitate an increase in the core's cross-sectional area (for non-gapped cores). Both of these options result in a higher transformer mass and/or volume. Additionally, a higher-than-necessary L_m may lower a transformer's resonant frequency enough that the intended TPIBC operating frequency is no longer tenable. As demonstrated in [47], the relationship between L_m and resonant frequency is given by

$$f_R = \frac{1}{2\pi\sqrt{L_m C_{tr}}} \tag{10}$$

where f_R is the transformer resonant frequency, L_m is its magnetization inductance, and C_{tr} is a total capacitance value. This value includes the capacitance between turns, between layers, and between windings.

A point worth noting is that making L_m larger by increasing the primary turns count will increase C_{tr} as well. In addition, the turns ratio will have a direct effect on C_{tr} [48]. Depending on the necessary L_m, it may be tricky to design a transformer with a low enough capacitance to achieve the wanted operating frequency and turns ratio. It is therefore desirable to select the minimum magnetizing inductance that still avoids DCM operation.

The turns ratio is chosen to be 8.5, and L_m is chosen to be 1 mH after performing PLECS simulations which showed the PPU functioning in CCM at this relatively high value of magnetization inductance. These simulations will be further discussed in Chapter 2.B; Table 2 contains the parameters associated with the PLECS simulation used to determine L_m, and Fig. 8 shows the simulation results illustrating that 1 mH is an appropriate value. The second plot of this figure shows that the boost inductor currents and magnetizing inductor current do not interfere with one another, which indicates that the DCM discussed in [41] has been avoided with this value of L_m. Otherwise-identical simulations performed at a lower L_m showed the PPU operating in that DCM, making 1 mH essentially the minimum necessary value. Given that the operating frequency was selected to be 100 kHz, a magnetization inductance of 1 mH limits C_{tr} to 2.53 nF.

v. VOLTAGE MULTIPLIER DESIGN

After selecting the transformer turns ratio, the CWVM stage count can be decided. The gain from a CWVM is given by

$$\frac{V_{out}}{V_{in_{pk}}} = 2N_s \tag{11}$$

where N_s is the number of CWVM stages and $V_{in_{pk}}$ is the peak voltage at the CWVM inputs. Given a total gain of 464, a nominal TPIBC duty of 70.6%, and a transformer turns ratio of 8.5, there is a remaining gain of 16 that must be handled by the CWVM. According to Eq. (11), this requires 8 CWVM stages.

For a CWVM which uses identical capacitors, the necessary capacitor voltage rating can be determined by

$$V_{c_{rating}} \geq \frac{V_{out}}{N_s} \tag{12}$$

where $V_{c_{rating}}$ is the capacitor voltage rating, V_{out} is the CWVM DC output voltage, and N_s is the number of CWVM stages.

The maximum CWVM output voltage can be determined by a total gain equation which does not include the post-CWVM voltage divider created by R_{lim}. This equation is expressed as:

$$\frac{V_{out}}{V_{in}} = \frac{2N_s}{1-d}\frac{N_2}{N_1} \tag{13}$$

This is simply the product of Eq. (2), (11), and the transformer turns ratio $\frac{N_2}{N_1}$. For the previously-established maximum TPIBC duty cycle of 87%, the maximum CWVM output voltage is 7.74 kV. Eq. (12) consequently establishes a minimum CWVM capacitor voltage rating of 968 V.

CWVMs exhibit two important characteristics that dictate a choice for capacitance: ripple and sag. Ripple refers to the magnitude of an AC signal which appears on a CWVM high-voltage DC output. Sag refers to the difference between the theoretical DC output voltage and the actual (lower) output voltage. From [26], the equation for determining CWVM output ripple is given as

$$\Delta V_{out} = \frac{I_{out}}{fC}\frac{N_s(N_s+1)}{2} \tag{14}$$

where ΔV_{out} is the ripple voltage, I_{out} is the output current, f is the CWVM input signal frequency, C is the capacitance of a CWVM capacitor (if they are all equal), and N_s is the stage count. Fig. 5 shows a sweep of capacitance values and the ripple voltages that result. This plot was generated for an 8-stage CWVM with an input voltage frequency of 100 kHz, as well as the nominal output current which results from the targeted CWVM output voltage (3.43 kV) and the nominal CWVM output resistance (9.74 MΩ).

The equation for CWVM output voltage sag[26] uses the same variables as Eq. (14), and is written as:

$$\delta V_{out} = \frac{I_{out}}{fC}\left(\frac{2N_s^3}{3} + \frac{N_s^2}{2} - \frac{N_s}{6}\right) \tag{15}$$

where δV_{out} is the output voltage difference between the no-load and loaded conditions. Fig. 5 graphically demonstrates the relationship between capacitance and voltage sag, using PPU parameters for 6-emitter nominal MEPS spray. 1 µF capacitors are chosen because they reduce the theoretical voltage sag to the point of single volts and they keep the theoretical CWVM output ripple to less than a volt. This level of control may be unnecessary however, and smaller capacitance values may also be perfectly acceptable according to the results of Fig. 5. Choosing a smaller capacitance value can also reduce the size of the PPU, which would be an essential consideration for a spaceflight-ready iteration of this PPU.

The presence of the current-limiting resistor R_{lim} shown in Fig. 3 creates a voltage divider with the thruster resistance. An adjustment to Eq. (13) is therefore necessary in order to predict the actual thruster voltage. The equation for thruster voltage can be written as follows:

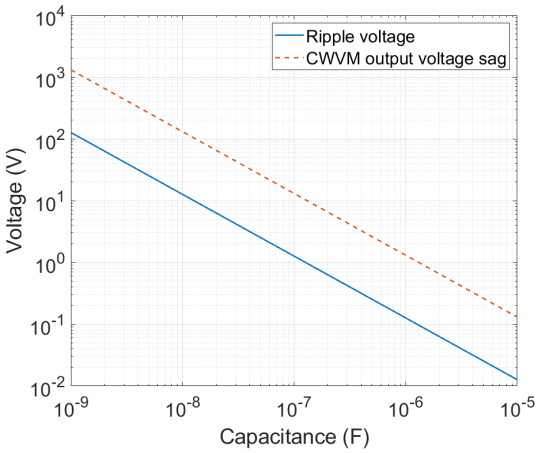

Fig. 5 Ripple and Sag at CWVM Output vs Capacitor Size

$$\frac{V_{out}}{V_{in}} = \frac{2N_s}{1-d}\frac{N_2}{N_1}\frac{R_{thrust}}{R_{thrust}+R_{lim}} \tag{16}$$

where V_{out} is the voltage delivered to the thruster, V_{in} is the PPU power supply voltage, N_s is the CWVM stage count, d is the TPIBC duty cycle, N_1 and N_2 are the transformer primary and secondary turn counts respectively, R_{lim} is the resistance of the current-limiting resistor, and R_{thrust} is the resistance of the thruster.

B. SIMULATIONS

i. SIMULATION WITH NOMINAL DUTY CYCLE AND THRUSTER RESISTANCE

PLECS simulations are used to predict the function and effectiveness of this electrospray PPU design. The first simulation performed was to verify PPU operation during unchanging nominal spray, which refers to the 6-emitter condition of $R_{thrust} = 350\,\text{M}\Omega$. A screenshot of the PLECS schematic is shown in Fig. 6. Table 2 contains the parameters used for this simulation. Two additional parameters are introduced in this table: $R_{DS(on)}$ (the drain-source resistance of a TPIBC MOSFET while conducting) and C_{DS} (the TPIBC MOSFET drain-source capacitance). In this PPU topology, C_{DS} serves a critical function by providing protection from inductive kickback, necessitating its inclusion in the simulation. In order to determine a approximate value for C_{DS}, a commercial MOSFET was selected and its datasheet used. After a review of its voltage and current ratings, the FDB12N50TM N-channel MOSFET from onsemi was chosen for this purpose.

The CWVM output voltage and thruster voltage were tracked over the course of the simulation and plotted in Fig. 7a. During steady-state, the mean thruster voltage was 3.21 kV (slightly lower than the 3.24 kV predicted

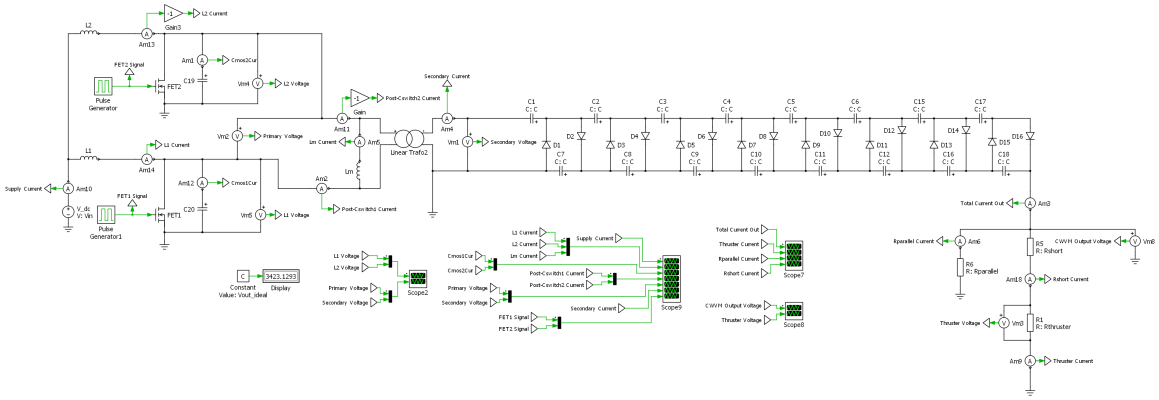

Fig. 6 PLECS Schematic of Electrospray PPU

Table 2 PLECS Simulation Parameters

V_{in}	7.4V
f	100 kHz
d	70.6%
L_{boost}	800 µH
N_2/N_1	8.5
L_m	1 mH
N_s	8
R_{thrust}	350 MΩ
R_{lim}	20 MΩ
R_{bleed}	10 MΩ
$R_{DS(on)}$	0.55 Ω
C_{DS}	128 pF

by Eq. (16)). The thruster voltage exhibited a peak-to-peak voltage of only 0.3 V during steady-state.

The currents produced by the PPU over the course of the fixed-R_{thrust} PLECS simulation are shown in Fig. 7b. During steady-state operation, the same 9.17 µA current flows through both the current-limiting resistor and the thruster. 349 µA is produced by the CWVM, most of which (approximately 339 µA) is delivered to R_{bleed}.

Fig. 8 contains several signals from this simulation which demonstrate the PPU's behavior throughout the topology. During steady-state operation, the average supply current drawn by the PPU was 164 mA with a peak-to-peak oscillation of 39 mA. It can be seen that the magnetization inductor current does *not* intersect either of the boost inductor current curves, though it comes quite close—this supports the use of $L_m \geq 1$ mH as a lower bound for transformer magnetizing inductance (as previously discussed in Chapter 2.A.iv). This minimum requirement for L_m may need raised if the PPU is to be used at off-nominal duty cycles, however[41].

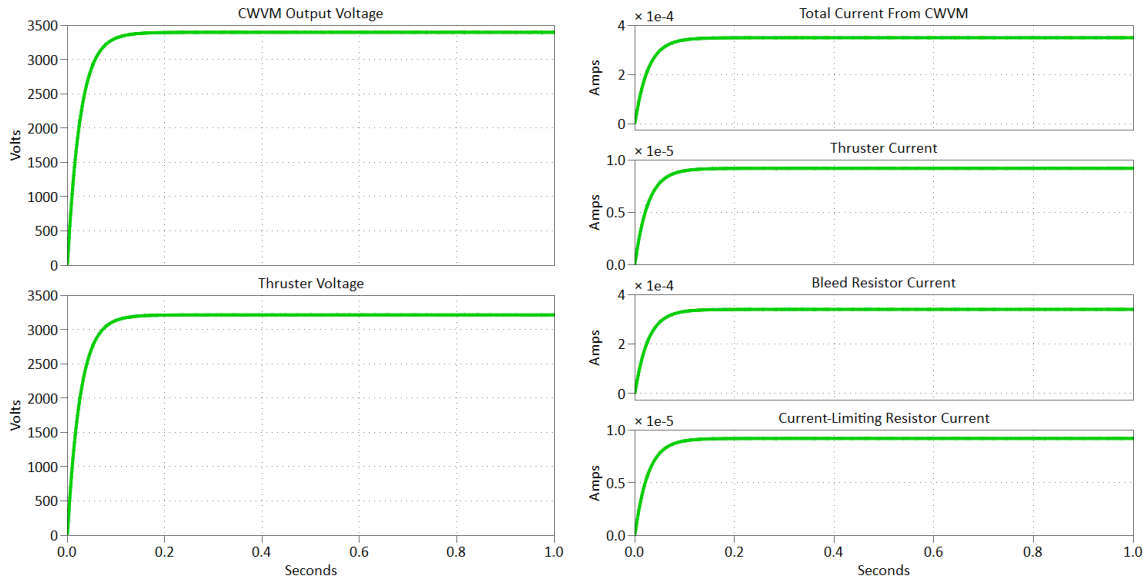

(a) Output Voltages **(b) Output Currents**

Fig. 7 Voltages and Currents Produced by Simulated Electrospray PPU with a Fixed Load

ii. VARIABLE-LOAD SIMULATION

A PLECS simulation was performed which tests PPU reliability given a more dynamic thruster resistance; the schematic used is shown in Fig. 9. The purpose of this simulation is to prove that the designed electrospray PPU will not be damaged during electrospray thruster startup (no-load condition) or during thruster shorts. This damage could potentially result from the generation of unexpectedly high output voltages or from unacceptably high power generation. Considering the CWVM will deliver approximately 1.2 W during nominal 6-emitter spray, an increase of more than a few watts may damage PPU components depending on their current ratings. When the actual ground-based prototype PPU is constructed, the variable-load tests performed in the simulation shown here will be replicated using the real hardware in order to verify its resilience before MEPS thruster application (the results of which are shown and discussed in Chapter 4.A.iii). Therefore, the method used in this simulation to test thruster startup and shorts was chosen because it can be easily replicated using real hardware.

The PPU in this simulation uses the same parameters as in Table 2, except for, of course, the thruster resistance. At simulation start, the node just before R_{thrust} is left disconnected from the rest of the circuit, which leaves R_{bleed} as the only load on the CWVM. This is intended to represent the no-load condition which occurs during MEPS thruster startup, as the MEPS thruster will not draw current until propellant has reached the emitter tips. After 1 second of simulation time, R_{thrust} is connected, with its resistance set to 350 MΩ (the

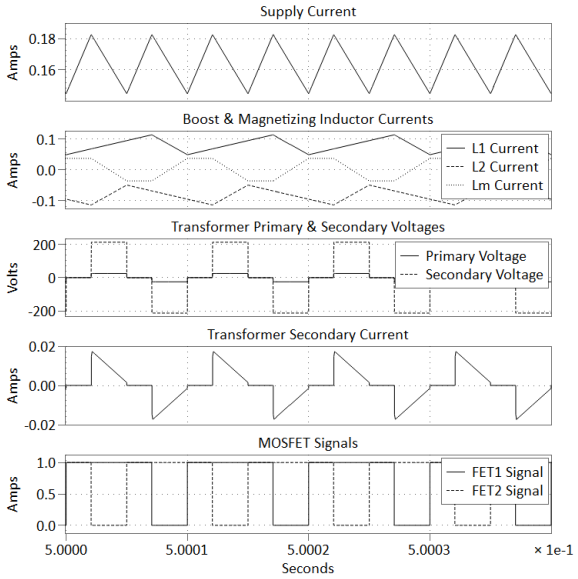

Fig. 8 PLECS-Simulated Electrospray PPU Intermediate Signals, for Fixed-Load Simulation

estimated value during nominal spray). One second later, in order to simulate the effect of a MEPS thruster short, a resistor is connected in parallel with R_{thrust} for a period of 10 ms. This decreases the value of the effective thruster resistance $R_{thrust_{eff}}$, which is defined as the equivalent resistance of R_{thrust} and any resistors placed in parallel with it (excluding R_{bleed}). $R_{thrust_{eff}}$ is abruptly decreased in this manner 3 times, for 10 ms at the start of each second. The first short is simulated by connecting a 30 MΩ resistor in parallel with R_{thrust}. During nominal, uninterrupted, 6-emitter spray, $R_{thrust_{eff}}$ is simply equal to R_{thrust}; the addition of this 30 MΩ resistor reduces $R_{thrust_{eff}}$ to about 1/10 its nominal value. The next short uses a 3 MΩ resistor instead, which cuts $R_{thrust_{eff}}$ down to approximately 1/100 of its nominal value. The final shorting test places

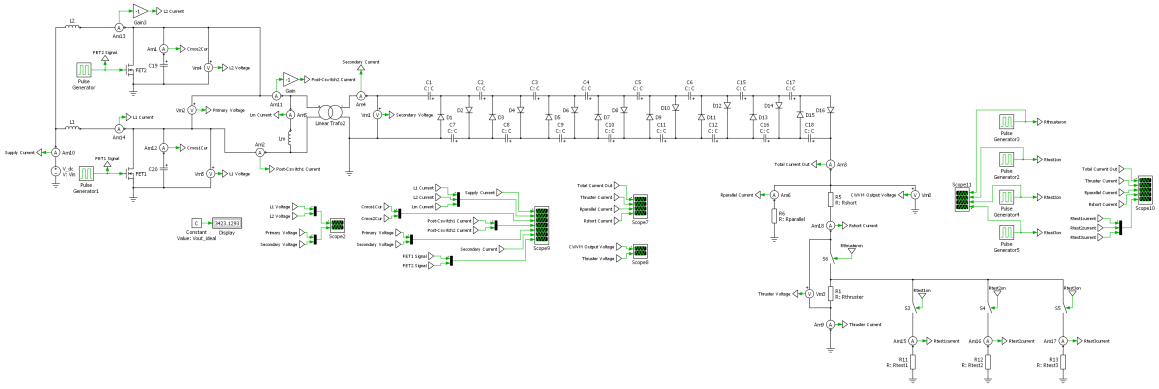

Fig. 9 PLECS Schematic of Electrospray PPU, for Variable-Load Simulation

a 300 kΩ resistor in parallel with R_{thrust}, which reduces $R_{thrust_{eff}}$ to approximately 1/1000 of its nominal value. Table 3 shows the value of $R_{thrust_{eff}}$ over the course of this simulation.

Table 3 Effective Thruster Resistance During a Variable-Load PLECS Simulation

t	$R_{thrust_{eff}}$
$0s - 1s$	∞
$1s - 2s$	350 MΩ
$2s - 2.01s$	27.6 MΩ
$2.01s - 3s$	350 MΩ
$3s - 3.01s$	2.97 MΩ
$3.01s - 4s$	350 MΩ
$4s - 4.01s$	299.7 kΩ
$4.01s - 5s$	350 MΩ

The PPU output voltages resulting from this variable-load simulation are displayed in Fig. 10a. Table 4 gives a quantitative summary of the shorts shown in the figure. The top plot in Fig. 10a demonstrates the PPU resilience in part. The CWVM output voltage is hardly affected by variation in $R_{thrust_{eff}}$, indicating that changes in the thruster condition will not cause abnormal or problematic PPU behavior. For every short, the CWVM output voltage drop is never more than a few volts. After the short, it recovers in a few tenths of a second to its pre-short mean. The CWVM output voltage is also not significantly affected by thruster startup, as it only drops by about 1.2 V when the 350 MΩ thruster is connected (when "spray" begins).

The thruster voltage drop, however, is quite significant during thruster shorts. The bottom plot in Fig. 10a shows that the thruster voltage falls dramatically during each short, falling further when $R_{thrust_{eff}}$ is lower. This result is due to the voltage divider created by R_{lim} and $R_{thrust_{eff}}$. The lower $R_{thrust_{eff}}$ is, the larger the voltage drop across R_{lim}. For the PPU design discussed in this paper, this is unavoidable; since the thruster current increases so much during a PPU short, maintaining the thruster voltage would require bursts of power that might place significant stress on the PPU's in-space power supply or damage PPU components. For example, during the third simulated short ($R_{thrust_{eff}}$ = 299.7 kΩ), maintaining the thruster voltage at 3.25 kV would require over 35 W to the thruster alone.

Table 4 Effects of Simulated Thruster Shorts

$R_{thrust_{eff}}$ (MΩ)	27.6	2.97	0.2997
CWVM output voltage loss (V)	2.2	5.3	5.7
CWVM output voltage recovery time (s)	0.16	0.18	0.20
Thruster voltage (multiplier of nominal)	0.613	0.137	0.0156

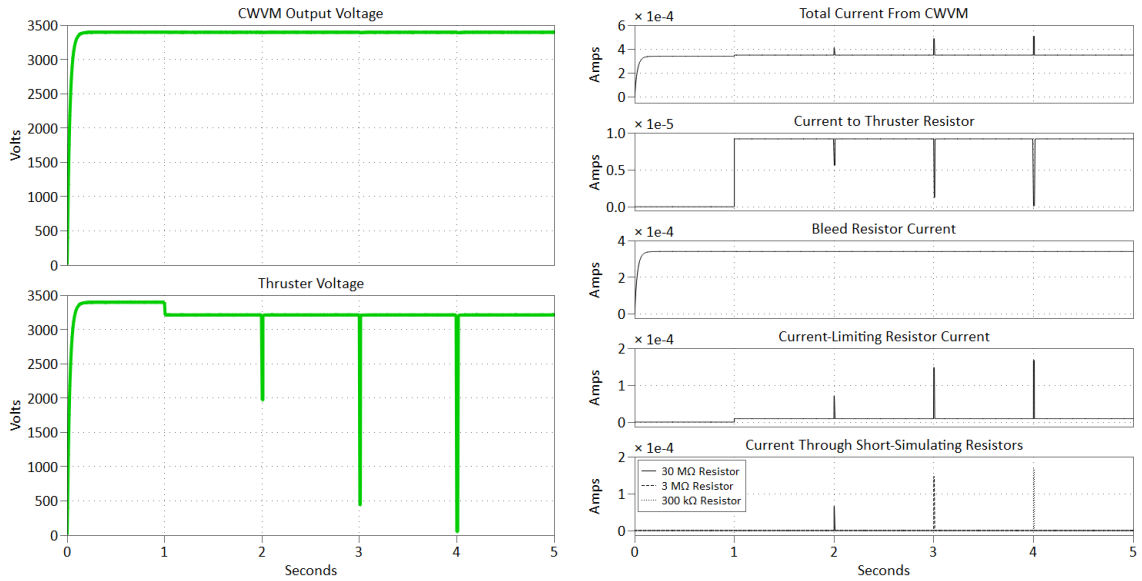

(a) Output Voltages **(b) Output Currents**

Fig. 10 Voltages and Currents Produced by Simulated Electrospray PPU with a Variable Load

The PPU resilience is further substantiated by the results shown in Fig. 10b. The top plot in this figure shows that for even the largest simulated drop in $R_{thrust_{eff}}$, the current from the CWVM does not rise to more than 510 µA, meaning the CWVM produces about 1.7 W during this time. This is the behavior intentionally created by the presence of R_{lim}, which protects components from overcurrent due to changes in the MEPS thruster's electrical load characteristics.

The PLECS simulations performed here indicate that R_{bleed} and R_{lim} successfully protect the PPU from both the very high thruster resistance occurring during thruster startup and the low thruster resistance occurring during emitter-extractor shorts. The CWVM output voltage remains quite stable, and the power delivery is properly limited to ensure the safety of PPU components.

CHAPTER 3: HARDWARE DEVELOPMENT

This section steps through the construction of the ground-based PPU in the topology order (TPIBC, transformer, then CWVM). Fig. 11 shows the constructed PPU used during all tests exhibited in Chapter 4.

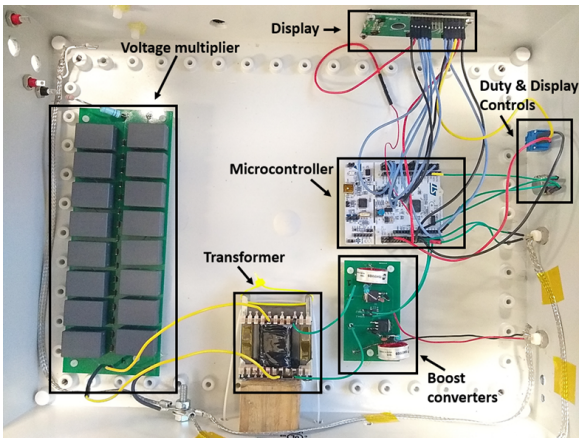

Fig. 11 Constructed PPU

Component selection was performed based on the previously-shown simulation results, which provided information on the maximum currents and voltages produced throughout the PPU. The components were not evaluated for their thermal performance, nor were the the component materials evaluated for their outgassing properties or radiation hardness. These would be essential steps towards qualifying future versions of this PPU for spacecraft use.

In addition to basic considerations of voltage and current limits, there are several other relevant parameters to consider when selecting TPIBC MOSFETs for this application. A low response time is desirable in order to reduce uncertainty on the TPIBC duty cycle. Minimizing gate charge and $R_{DS_{on}}$ can help reduce switching and conduction losses[42]. Most importantly, C_{DS} should be minimized in order to prevent ringing with the transformer leakage inductance. Though this ringing is unwanted, C_{DS} does serve an important purpose as a transition buffer in the TPIBC (as discussed in Chapter 2.B)—it prevents inductive kickback as a result of a current discontinuity that would otherwise be created during TPIBC MOSFET transitions. A real-world MOSFET has already been chosen during the design process in order to get an estimate of C_{DS} for PLECS simulation purposes. The FDB12N50TM N-channel MOSFET from onsemi was found to be suitable. Its V_{DS} rating of 500 V and its drain current (I_D) rating of 6.9 A (at 100 °C) are both much higher than the currents and voltages which will be generated in the TPIBC. A MIC4424 was chosen to drive these MOSFETs, as it can still be properly triggered even if the STM32 microcontroller produces only 3.3 V signals.

The electrospray PPU TPIBC uses two 800 µH inductors. They were chosen to be well above the 289 µH required for continuous conduction mode operation, as described by Eq. (8). The PPU mass could be reduced by reducing the factor of safety on inductor sizing, which should be considered when moving beyond this ground-based PPU prototype.

The microcontroller which sends signals to drive the TPIBC MOSFET gates must be able to produce 100 kHz square pulses and provide a sufficient resolution of control over their duty cycle (for PPU output voltage control). The STM32 L476RG Nucleo board was selected for this role, in part for the additional features it offers. The board has many unused pins even after it was readied for MOSFET control signal generation, meaning it can be used to serve auxiliary functions within the PPU as the need for them arises (such as those shown in Fig. 1). Its ADC features make it capable of performing closed-loop PPU output voltage control, which is a possible addition in future iterations of this PPU (and likely necessary for spacecraft application). It also accepts several power supply options including external 3.3 V and USB.

Some of the aforementioned extra microcontroller pins were put to use for manual voltage control and a small LCD display. For voltage control, a potentiometer knob was made accessible from the outside of the PPU case. The potentiometer forms part of a voltage divider, the analog output of which is sent to a microcontroller pin. The microcontroller turns this small voltage signal into a value for the TPIBC duty cycle, giving the user real-time control over the PPU output voltage. The duty cycle and predicted output voltage are shown on a small LCD screen (also powered by the microcontroller) in order to give feedback to the user. This is useful for open-loop ground-based testing, though this functionality would of course be removed for a closed-loop in-space version of the PPU.

The custom transformer was constructed on an E55/28/21 core with a turns ratio of 1:8.57. Its resonant frequency was measured to be 122 kHz. This is fairly close to the operating frequency, which means the operating frequency cannot be increased very much without needing to construct a new transformer. Measurements of the magnetization inductance taken at frequencies of 10 kHz and below showed it to be 1.22 mH, just above the minimum necessary value of 1 mH. However, measuring the magnetization inductance at 100 kHz shows $L_m = 4.90$ mH, much larger than the required 1 mH. The apparent increase in magnetization inductance at 100 kHz is likely the result of the close proximity between the operating and resonant frequencies, an effect commonly seen in inductors due to their self-capacitance and referred to there as self-resonance.

Simple RC snubbers were added across the drain and source of each TPIBC MOSFET, to reduce ringing between the MOSFET drain-source capacitance and the transformer leakage inductance (measured to be 2.8 µH). Each snubber used a 47 Ω resistor and a 3 nF capacitor.

The 8-stage CWVM was built using 1 µF film capacitors. Multi-layer ceramic capacitors (MLCCs) were considered but rejected for the purpose of this ground-based PPU prototype, as their voltage coefficient of capacitance effect combined with the required voltage rating was a combination that seemed likely to produce capacitance derating, causing the CWVM output voltage to ripple more than expected. Using MLCCs would likely significantly decrease the PPU size, and should be considered when building a flight version of this PPU. A comparison of two CWVMs built at EPLab is shown in Fig. 12, exhibiting the size difference between MLCC and film capacitors.

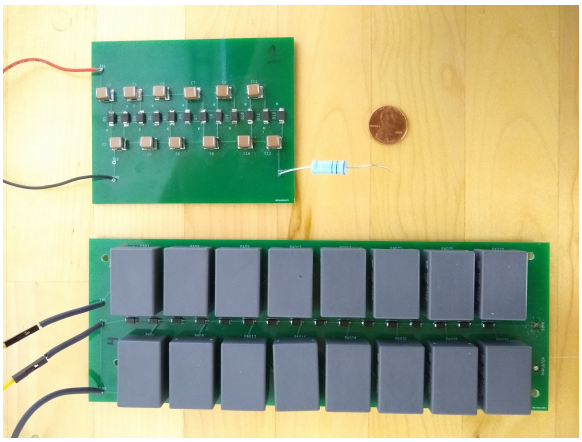

Fig. 12 Size Comparison of 6-Stage CWVM Built with MLCCs (Top) and 8-Stage CWVM Built with Film Capacitors (Bottom). Penny for Scale.

CHAPTER 4: EXPERIMENTAL RESULTS

A. STANDALONE PPU TESTING

The purpose of these standalone tests is to verify the PPU behavior before integrating it with the MEPS thruster. This includes its output voltage (measured at several duty cycles), its efficiency, and its response to the no-load and short conditions meant to represent MEPS thruster startup and shorts. During these standalone tests, the CWVM output voltage is measured. In order to accomplish this, a 100 kΩ metal film resistor is placed in series with the 10 MΩ R_{bleed}, and a Tektronix P2221 voltage probe is placed across that 100 kΩ resistor. The Tektronix DPO2024 oscilloscope used for these measurements has an input impedance of 1 MΩ. Though this is not a direct measurement of the voltage being applied to the thruster, the thruster voltage can be inferred via the CWVM output voltage as described by Eq. (16).

i. TEST WITH NOMINAL DUTY CYCLE AND THRUSTER RESISTANCE

For the first test of the standalone PPU, the TPIBC duty cycle is fixed at its nominal value of 70.6% and the PPU input voltage is set to 7.4 V DC. A 350 MΩ resistor bank is placed after the 20 MΩ current-limiting resistors in order to simulate the MEPS thruster's nominal electrical impedance during 6-emitter spray. A graphical depiction of the PPU loading and measurement configuration can be seen in Fig. 13.

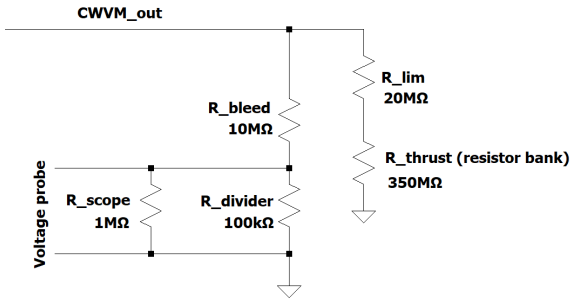

Fig. 13 Loading and Measurement at PPU Output, for Standalone Tests with Nominal Thruster Resistance

The mean CWVM output voltage is 3.38 kV, with a peak-to-peak ripple of 198 V and a standard deviation of 55 V. Fig. 14 shows the ripple characteristics of the CWVM output voltage. This ripple is significantly more than the 0.3 V predicted by the simulation performed in 2.B.i. One possible explanation for its presence is a grounding issue; as shown in [31], its shape is very similar to the ripple seen in a previous iteration of the PPU design where neither CWVM input was grounded. Though the PPU explored in this paper is the updated

version (with one CWVM input held at ground), it is possible that this ground connection was tenuous enough to reproduce the unwanted ripple.

Once the 7.4 V PPU input power was turned off, the CWVM output voltage fell over the course of approximately 13 seconds before reaching roughly zero. This can be considered the PPU's necessary turn-off time. The turn-on time, however, was not measured. The PPU draws a large amount of current during this turn-on time, which was consequently limited by the input power supply in order to prevent damage to PPU components. This current-limiting during turn-on of course affects the apparent turn-on time. A spaceflight-ready iteration of this PPU would need to employ a more deliberate solution for mitigating inrush current.

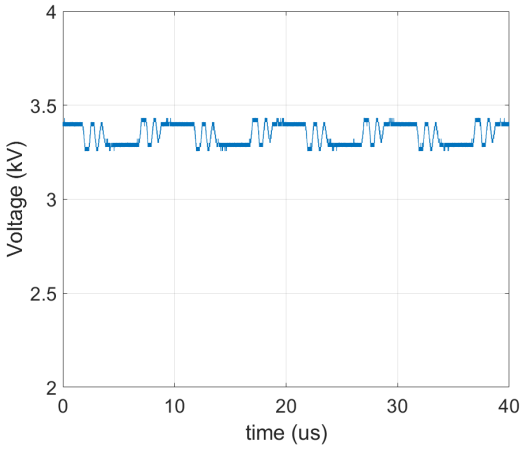

Fig. 14 CWVM Output Voltage Ripple

ii. DUTY CYCLE SWEEP

The PPU hardware was run at several duty cycles and the CWVM output voltage observed. This test of the standalone PPU used the same loading and measurement configuration shown in Fig. 13. The results of this duty cycle sweep are summarized in Table 5. For each duty cycle, the table shows the mean CWVM output voltage (and its corresponding standard deviation σ and peak-to-peak value), the power demanded at the PPU input, the power produced at the CWVM output, and the efficiency η. Here, η is defined as the ratio between the mean power delivered by the CWVM and the PPU input power. Note that because R_{bleed} (10 MΩ) is so much smaller than R_{thrust} (350 MΩ), most of the CWVM output power is not actually delivered to the thruster. A very similar PPU built in [31] was shown to achieve up to about 63% efficiency. Other electrospray PPU topologies shown in [30], [49], and [35] demonstrated efficiencies of up to 85.57%, 88.5%, and 80.4%

Table 5 Duty Cycle Sweep Results

Duty	Mean Voltage (kV)	σ (V)	pk-pk (V)	P_{in} (Mean) (W)	CWVM P_{out} (Mean) (W)	η (%)
0.550	2.21	42	154	1.65	0.495	30.0
0.600	2.49	46	176	2.68	0.631	23.5
0.650	2.74	58	242	3.02	0.765	25.3
0.700	3.22	56	198	5.16	1.05	20.4
0.746	3.43	59	198	5.84	1.20	20.6

(respectively). The PPU developed in [34] achieved an efficiency of up to 73%, though this peak efficiency occurred at a higher output power than their target; the efficiency at their target power was measured to be 36%. As seen in Table 5, the electrospray PPU developed here for MEPS achieves its peak efficiency of 30% at its lowest allowable duty cycle (0.550), and only achieves an efficiency of about 20% near the duty cycle targeted for nominal MEPS operation (0.706 as established in Chapter 2.A.iii). Losses can be primarily attributed to power dissipation in the RC snubbers, TPIBC MOSFET switching losses, transformer core and resistive losses, and losses in the CWVM diodes. An alternative (less-lossy) snubbing solution should be employed in further iterations of this PPU to improve its efficiency.

Fig. 15 compares the mean CWVM output voltages produced by the PPU to the voltages expected from Eq. (13). As duty cycle increases, the voltages produced by the real PPU fall further below the ideal curve. This may be attributed to the losses in TPIBC gain which occur at higher duty cycles, as described in Eq. (5).

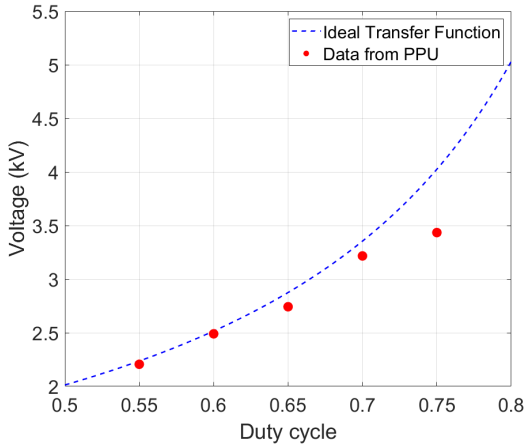

Fig. 15 PPU Output Voltage at Tested Duty Cycles Compared to Ideal Output Voltage

iii. VARIABLE-LOAD TEST

The standalone PPU was tested for its ability to survive the fluctuations in thruster resistance which occur during MEPS thruster startup and shorts. The PPU loading and measurement configuration for this test is summarized by Fig. 16.

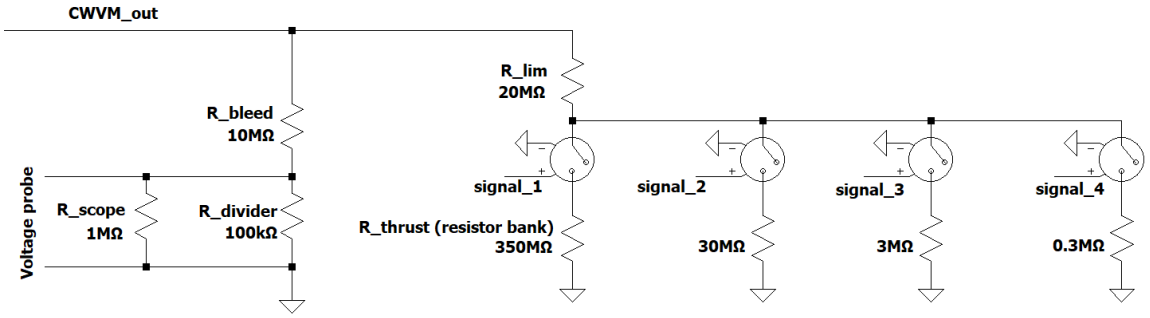

Fig. 16 Loading and Measurement at PPU Output, for Standalone Tests with Variable Thruster Resistance

This hardware test replicates the variable-load simulation performed in Chapter 2.B.ii. As in that simulation, the PPU is turned on without any thruster-emulating resistors connected at the PPU output. This represents the no-load condition that would exist during MEPS thruster startup; as the propellant takes some time to reach the emitter tips, the thruster will not immediately draw current from the PPU. After several seconds (once the CWVM output voltage reached steady-state), the 350 MΩ resistor bank (R_{thrust}) is connected at the PPU output by activating a high-voltage relay. Again, this approximately represents the MEPS thruster's nominal electrical resistance during 6-emitter electrospray operation. One second later, for a 10 ms period, an additional high-voltage relay is activated which connects a 3 MΩ resistor in parallel with the 350 MΩ resistor bank. For this 10 ms period, the effective thruster resistance is consequently reduced to about 1/10 its nominal value. As defined in Chapter 2.B.ii, the effective thruster resistance $R_{thrust_{eff}}$ refers to the equivalent resistance of R_{thrust} and any resistors placed in parallel with it (excluding the bleeder resistor R_{bleed} and any resistors associated with CWVM voltage measurement, such as the $R_{divider}$ and R_{scope} seen in Fig. 16). One second later, $R_{thrust_{eff}}$ is decreased again for a 10 ms period, this time using a 3 MΩ resistor. After another second, $R_{thrust_{eff}}$ is decreased one final time for a 10 ms period, using a 0.3 MΩ resistor. The purpose of these drops in $R_{thrust_{eff}}$ are to emulate the sudden decreases in MEPS thruster resistance that sometimes occur during emitter-extractor shorts.

An Arduino Nano was used to trigger each of the DAT70510 high-voltage relays (with MOSFET buffers used in-between the Arduino signals and the relay gates in order to supply the necessary gate currents). Fig. 17

shows the hardware used to create a variable load on the PPU output.

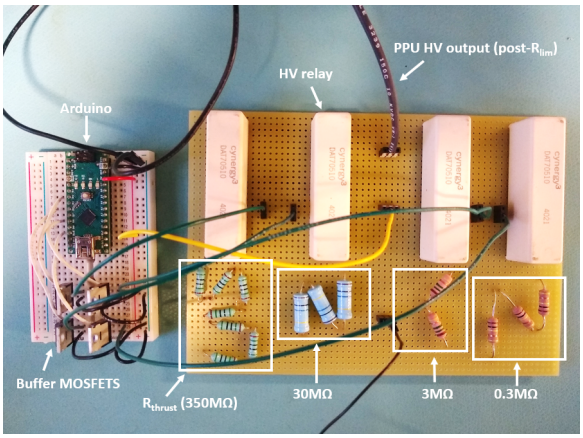

Fig. 17 Hardware for Variable-Load Testing of Standalone PPU

The PPU input voltage was set to 7.4 V and the TPIBC duty cycle to 70.6%. Several seconds after the PPU was started up, the CWVM output voltage stabilized at 3.41 kV under this no-load condition. After the 350 MΩ resistor bank (R_{thrust}) was connected by activating its associated relay, the CWVM mean output voltage was found to have dropped by only 0.6 V—a near-negligible result considering the CWVM output voltage had a standard deviation of 53 V over the course of this test. This result suggests the PPU is able to produce a consistent output voltage both during and after the electrospray thruster startup period.

As for the short-emulating tests occurring over the several seconds following the attachment of R_{thrust}, Fig. 18 summarizes the results. When compared to the simulation results shown in Table 4, the CWVM output voltage drops seen in the real PPU are very similar (only a few volts each time). Only one tested short produced a voltage drop larger than the simulated drop, at 6.9 V compared to 5.7 V; again, considering the CWVM output voltage had a standard deviation of 53 V over the course of the test, the drop in mean voltage is relatively small. These results indicate the CWVM output voltage remains stable even when the thruster resistance drops to less than 1/1000 its nominal value (as it might during an electrospray thruster short). These tests therefore validate the simulations performed in Chapter 2.B.ii, showing that the PPU produces a reliable output voltage when the thruster resistance is near-infinite (as it is during electrospray thruster startup), when the thruster resistance is at its nominal value for 6-emitter spray, and when the thruster resistance drops by several orders of magnitude as it might during electrospray thruster shorts. A further PPU test was performed with the output of R_{lim} connected directly to ground (a complete short); though no data was taken from this test, no PPU components suffered obvious damage and the PPU continued to perform nominally during subsequent uses. The PPU hardware was therefore shown to survive the full range of load conditions (no-load to complete

short), proving itself resilient enough for use with the load conditions which might be presented by an actual electrospray thruster.

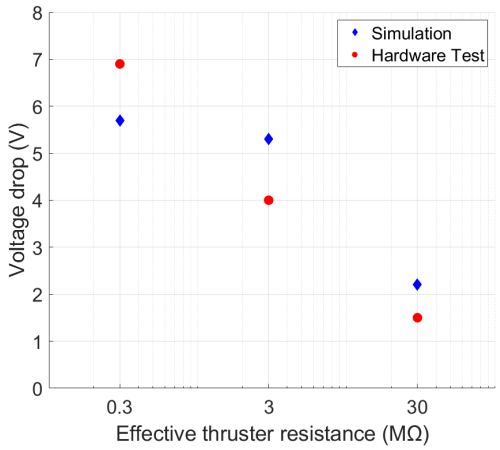

Fig. 18 CWVM Voltage Drop Resulting From Short-Emulating Test, Compared to Simulation

B. LONG-DURATION TEST OF PPU

Prior to full integration with the MEPS thruster, the electrospray PPU was left to run at a constant duty cycle of 70% for almost 10.5 hours, with the input voltage set to 7.4 V. For this test, the CWVM output voltage was reduced by a factor of 1000 via a voltage divider, and this reduced voltage was sensed by an instrumentation amplifier (set with a gain of 1). A schematic of the PPU loading and measurement setup is shown in 19.

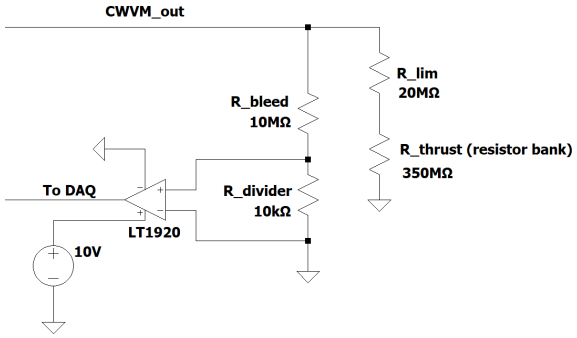

Fig. 19 Loading and Measurement at PPU Output, for Long-Duration Test

The CWVM output voltage over the course of this long-duration run is shown in Fig. 20. A moving average with a span of one minute was applied to this data to improve readability. By Eq. (13), a mean voltage of 3.35 kV was expected. Fig. 20 shows that the actual CWVM produced a mean voltage of 3.27 kV, which

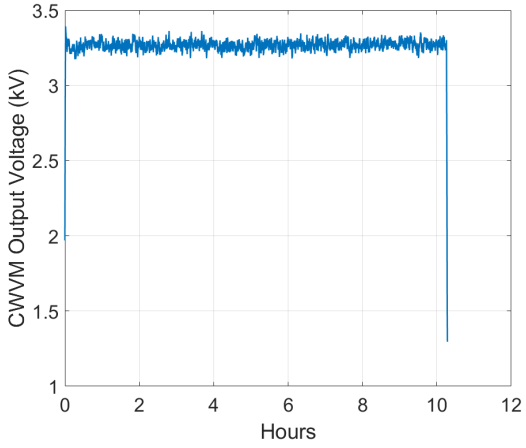

Fig. 20 Electrospray PPU CWVM Output Voltage During Long-Duration Test (Moving Average)

stayed fairly stable over the course of the test. The non-averaged test data had a standard deviation of 204 V and a peak to peak voltage of 1.38 kV over the course of the run. The likely cause of this unexpectedly high peak-to-peak voltage was later determined to be the 10 kΩ resistor used in the voltage divider measurement path. This resistor's material was carbon film, experimentally shown to have a less-stable resistance value and increased current noise when compared to metal film resistors[50, 51]. This resistor was later replaced with a 100 kΩ metal film resistor in order to generate the data shown in Chapter 4.A, which significantly reduced the ripple observed in PPU output voltage during standalone PPU tests.

C. ELECTROSPRAY THRUSTER TEST WITH PPU

After the long-duration test was conducted, the PPU was integrated with the MEPS thruster for an application demo. During this test, a 2-input switchbox controlled the voltage polarity of the extractor; one input was the positive high voltage provided by the PPU, and the other input was a negative high voltage provided by a commercial power supply. The extractor voltage was switched between these two sources every 5 seconds.

Fig. 21 shows the positive MEPS extractor voltage produced by the PPU over the course of several polarity-switching cycles. The data for negative extractor voltage is not shown here for clarity's sake; since it was produced by a commercial power supply and not the PPU, it does not demonstrate anything about the PPU itself.

The commercial power supply was set to provide a fixed voltage of −3.25 kV. The PPU power supply was set to 7V and the duty cycle to 70.75%. Eq. (16) therefore predicts a positive thruster voltage of 3.25 kV during

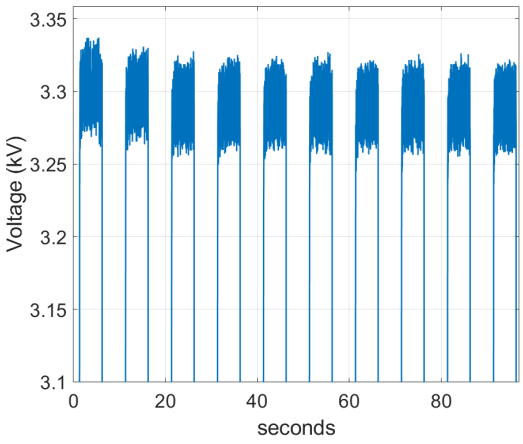

Fig. 21 Positive EPS Extractor Voltage During PPU Application Demo

nominal spray (with the estimated R_{thrust} of 350 MΩ). The actual mean positive voltage (the mean voltage delivered by the PPU to the thruster) was calculated to be 3.27 kV while the thruster sprayed, with a standard deviation of 156 V. This standard deviation is larger than the CWVM output voltage standard deviation of 55 V found during the standalone PPU test described in 4.A.i.

The test was manually ended after about 45 minutes of thruster spray due to time constraints (it was not ended by any hardware failure, such as a short due to emitter-side flooding). Over the course of this spray time, 5 out of the 6 open emitter channels became simultaneously active, forming Taylor cones from which propellant was sprayed. Despite the higher-than-expected thruster voltage standard deviation, the thruster turned on and sprayed successfully, and the mean thruster voltage remained stable over the course of the test. Successfully integrating a ground-based custom electrospray PPU with the MEPS thruster represents a significant step towards eventual MEPS flight-readiness.

CHAPTER 5: CONCLUSION

For the first time, a custom-built electrospray PPU has been successfully used to spray with a multimode monopropellant-electrospray thruster. Modifying a preexisting PPU topology allowed it to meet the needs of the MEPS thruster. This thruster test verified analytical and simulated results which indicated the PPU topology was an appropriate fit for MEPS application. In particular, the topology overcame the highly-variable load inherent to electrospray thruster operation, which results from no-load conditions during thruster startup and the short conditions resulting from unwanted emitter-extractor electrical bridging. The topology was able to provide a reliable mean output voltage during that startup period as well as a safe power output during shorts. Though the design, simulations, and hardware focused on suitability for MEPS thruster spray in its 6-emitter configuration, the PPU can be tweaked for compatibility with the MEPS thruster when more of (or all of) the 256 emitters are active.

Building a transformer to avoid converter DCM while also operating at the interleaved boost converter switching frequency was a non-trivial task for this low-power application. This consideration potentially makes transformer-less designs preferable from a practical standpoint, though electrospray thrusters operating in the range of several watts will be less likely to create this design hurdle. This means transformer design and construction would potentially be easier for full-emitter-array spray with the MEPS thruster than it was for 6-emitter spray.

Significant improvements can be made to the PPU itself, such as bringing its efficiency up to par with other existing electrospray topologies, implementing closed-loop output voltage control, and reducing its mass and volume via component re-selections. Though the topology's allowance for grounded emitters is a plus due to the difficulty of electrically isolating the propellant, a floating ground configuration may be deemed necessary in the future for charge-balancing purposes.

The near-endless topology space for high-voltage generation means that electrospray PPU designers have a wide variety of options; however, very few of those topologies have been examined for compatibility with electrospray thruster use, and even fewer have been tested with an actual thruster. The work presented here helps increase the amount of custom converter options available to other electrospray PPU designers.

REFERENCES

[1] Rovey, J. L., Lyne, C. T., Mundahl, A. J., Rasmont, N., Glascock, M. S., Wainwright, M. J., and Berg, S. P., "Review of multimode space propulsion," *Progress in Aerospace Sciences*, Vol. 118, 2020, p. 100627. https://doi.org/https://doi.org/10.1016/j.paerosci.2020.100627.

[2] Kopacz, J. R., Herschitz, R., and Roney, J., "Small satellites an overview and assessment," *Acta Astronautica*, Vol. 170, 2020, pp. 93–105. https://doi.org/https://doi.org/10.1016/j.actaastro.2020.01.034.

[3] Berg, S. P., and Rovey, J. L., "Assessment of Multimode Spacecraft Micropropulsion Systems," *Journal of Spacecraft and Rockets*, Vol. 54, No. 3, 2017, pp. 592–601. https://doi.org/10.2514/1.A33649.

[4] Falcone, G., Engel, D. L., Cortinovis, M., Ryan, C. N., Rovey, J. L., Putnam, Z. R., Berg, S., and Lembeck, M., "Mission Performance Assessment of Multimode Propulsion for Satellite Servicing Applications," *2022 IEEE Aerospace Conference (AERO)*, 2022, pp. 1–19. https://doi.org/10.1109/AERO53065.2022.9843839.

[5] Rexius, T., and Holmes, M., *Mission Capability Gains from Multi-Mode Propulsion Thrust Profile Variations for a Plane Change Maneuver*, 2012. https://doi.org/10.2514/6.2011-6431.

[6] Cline, B., Berg, S., and Rovey, J., *Preliminary Screening of Multimode Spacecraft Propulsion Systems for Interplanetary Missions*, 2021. https://doi.org/10.2514/6.2022-1354.

[7] Bruno, A., Schroeder, M., and Lozano, P. C., *Characterization of Electrospray Thrusters with HAN-Based Monopropellants for Multimode Propulsion Applications*, 2022. https://doi.org/10.2514/6.2022-2490.

[8] GUO, Y., SUN, W., SUN, Z., WU, Z., HE, J., YANG, C., and WANG, N., "Direct thrust test and asymmetric performance of porous ionic liquid electrospray thruster," *Chinese Journal of Aeronautics*, 2022. https://doi.org/https://doi.org/10.1016/j.cja.2022.09.007.

[9] Powaser, A. M., and Greig, A. D., "Colloid Thruster to Teach Advanced Electric Propulsion Techniques to Undergraduates," *2018 Joint Propulsion Conference*, 2018, p. 4711.

[10] Courtney, D. G., Dandavino, S., and Shea, H., "Comparing Direct and Indirect Thrust Measurements from Passively Fed Ionic Electrospray Thrusters," *Journal of Propulsion and Power*, Vol. 32, No. 2, 2016, pp. 392–407. https://doi.org/10.2514/1.B35836.

[11] Courtney, D. G., Wood, Z., Gray, S., and Model, J., "High-speed transient characterization of the busek BET-300-P electrospray thruster," *36th International Electric Propulsion Conference, Vienna, Austria*, 2019.

[12] Velásquez-García, L., and Fernando, L., "The design, fabrication and testing of micro-fabricated linear and planar colloid thruster arrays," 2005.

[13] Anderson, G., Anderson, J., Anderson, M., Aveni, G., Bame, D., Barela, P., Blackman, K., Carmain, A., Chen, L., Cherng, M., Clark, S., Connally, M., Connolly, W., Conroy, D., Cooper, M., Cutler, C., D'Agostino, J., Demmons, N., Dorantes, E., Dunn, C., Duran, M., Ehrbar, E., Evans, J., Fernandez, J., Franklin, G., Girard, M., Gorelik, J., Hruby, V., Hsu, O., Jackson, D., Javidnia, S., Kern, D., Knopp, M., Kolasinski, R., Kuo, C., Le, T., Li, I., Liepack, O., Littlefield, A., Maghami, P., Malik, S., Markley, L., Martin, R., Marrese-Reading, C., Mehta, J., Mennela, J., Miller, D., Nguyen, D., O'Donnell, J., Parikh, R., Plett, G., Ramsey, T., Randolph, T., Rhodes, S., Romero-Wolf, A., Roy, T., Ruiz, A., Shaw, H., Slutsky, J., Spence, D., Stocky, J., Tallon, J., Thorpe, I., Tolman, W., Umfress, H., Valencia, R., Valerio, C., Warner, W., Wellman, J., Willis, P., Ziemer, J., Zwahlen, J., Armano, M., Audley, H., Baird, J., Binetruy, P., Born, M., Bortoluzzi, D., Castelli, E., Cavalleri, A., Cesarini, A., Cruise, A., Danzmann, K., de Deus Silva, M., Diepholz, I., Dixon, G., Dolesi, R., Ferraioli, L., Ferroni, V., Fitzsimons, E., Freschi, M., Gesa, L., Gibert, F., Giardini, D., Giusteri, R., Grimani, C., Grzymisch, J., Harrison, I., Heinzel, G., Hewitson, M., Hollington, D., Hoyland, D., Hueller, M., Inchauspé, H., Jennrich, O., Jetzer, P., Karnesis, N., Kaune, B., Korsakova, N., Killow, C., Lobo, J., Lloro, I., Liu, L., López-Zaragoza, J., Maarschalkerweerd, R., Mance, D., Meshksar, N., Martín, V., Martin-Polo, L., Martino, J., Martin-Porqueras, F., Mateos, I., McNamara, P., Mendes, J., Mendes, L., Nofrarias, M., Paczkowski, S., Perreur-Lloyd, M., Petiteau, A., Pivato, P., Plagnol, E., Ramos-Castro, J., Reiche, J., Robertson, D., Rivas, F., Russano, G., Sopuerta, C., Sumner, T., Texier, D., Vetrugno, D., Vitale, S., Wanner, G., Ward, H., Wass, P., Weber, W., Wissel, L., Wittchen, A., and Zweifel, P., "Experimental results from the ST7 mission on LISA Pathfinder," *Physical Review D*, Vol. 98, No. 10, 2018. https://doi.org/10.1103/physrevd.98.102005.

[14] Berg, S., and Rovey, J., *Ignition Evaluation of Monopropellant Blends of HAN and Imidazole-Based Ionic Liquid Fuels*, 2012. https://doi.org/10.2514/6.2012-974.

[15] Berg, S. P., and Rovey, J. L., "Decomposition of Monopropellant Blends of Hydroxylammonium Nitrate and Imidazole-Based Ionic Liquid Fuels," *Journal of Propulsion and Power*, Vol. 29, No. 1, 2013, pp. 125–135. https://doi.org/10.2514/1.B34584.

[16] Berg, S. P., and Rovey, J., *Decomposition of a Double Salt Ionic Liquid Monopropellant in a Microtube for Multi-Mode Micropropulsion Applications*, 2017. https://doi.org/10.2514/6.2017-4755.

[17] Berg, S., Glascock, M., Jones, F., and Rovey, J., "Experimental and Modeling Results for the Chemical Mode of an Integrated Multimode Thruster," *Joint Army Navy NASA Air Force (JANNAF) 10th Space Propulsion Joint Subcommittee Meeting, Tampa, FL.*, 2019.

[18] Lyne, C. T., Rovey, J., and Berg, S. P., *Monopropellant-Electrospray Multimode Thruster Testing Results: Electrospray Mode*, 2021. https://doi.org/10.2514/6.2021-3439.

[19] Mier-Hicks, F., and Lozano, P. C., "Spacecraft-Charging Characteristics Induced by the Operation of Electrospray Thrusters," *Journal of Propulsion and Power*, Vol. 33, No. 2, 2017, pp. 456–467. https://doi.org/10.2514/1.B36292.

[20] Lozano, P., and Martínez-Sánchez, M., "Ionic liquid ion sources: suppression of electrochemical reactions using voltage alternation," *Journal of Colloid and Interface Science*, Vol. 280, No. 1, 2004, pp. 149–154. https://doi.org/https://doi.org/10.1016/j.jcis.2004.07.037.

[21] Mier Hicks, F., "Characterization on a magnetically levitated testbed for electrospray propulsion systems," Ph.D. thesis, Massachusetts Institute of Technology, 2014.

[22] Thuppul, A., Wright, P. L., Collins, A. L., Ziemer, J. K., and Wirz, R. E., "Lifetime Considerations for Electrospray Thrusters," *Aerospace*, Vol. 7, No. 8, 2020. https://doi.org/10.3390/aerospace7080108.

[23] Gamero-Castaño, M., and Galobardes-Esteban, M., "Electrospray propulsion: Modeling of the beams of droplets and ions of highly conducting propellants," *Journal of Applied Physics*, Vol. 131, No. 1, 2022, p. 013307. https://doi.org/10.1063/5.0073380.

[24] Savytskyy, I., and Jugroot, M., *Design and Modeling of a Vectored Electrospray Thruster*, 2022. https://doi.org/10.2514/6.2022-4271.

[25] Howe, D. R., "Design of and Electrospray Thruster Power Processing and Digital Control Interface Unit," Master's thesis, California Polytechnic State University, 2020.

[26] Abdel-Salam, M., Anis, H., El-Morshedy, A., and Radwan, R., *High-Voltage Engineering: Theory and Practice*, Marcel Dekker, New York, 2000.

[27] Hossain, M., Rahim, N., and a/l Selvaraj, J., "Recent progress and development on power DC-DC converter topology, control, design and applications: A review," *Renewable and Sustainable Energy Reviews*, Vol. 81, 2018, pp. 205–230. https://doi.org/https://doi.org/10.1016/j.rser.2017.07.017.

[28] Tofoli, F. L., Pereira, D. d. C., Josias de Paula, W., and Oliveira Júnior, D. d. S., "Survey on non-isolated high-voltage step-up dc–dc topologies based on the boost converter," *IET Power Electronics*, Vol. 8, No. 10, 2015, pp. 2044–2057. https://doi.org/https://doi.org/10.1049/iet-pel.2014.0605.

[29] Veeramraju, K. J. P., "Design and Development of Power Processing Units for Applications in Electrically-Propelled Satellite Systems," Master's thesis, Missouri University of Science and Technology, 2020.

[30] Baddipadiga, B. P., Strathman, S., Ferdowsi, M., and Kimball, J. W., "A high-voltage-gain DC-DC converter for powering a multi-mode monopropellant-electrospray propulsion system in satellites," *2018 IEEE Applied Power Electronics Conference and Exposition (APEC)*, 2018, pp. 1561–1565. https://doi.org/10.1109/APEC.2018.8341224.

[31] Prasad Veeramraju, K. J., and Kimball, J. W., "An Improved Power Processing Unit for Multi-Mode Monopropellant Electrospray Thrusters for Satellite Propulsion Systems," *2019 IEEE Energy Conversion Congress and Exposition (ECCE)*, 2019, pp. 1302–1309. https://doi.org/10.1109/ECCE.2019.8913026.

[32] Hruby, V., Gamero-Castano, M., Spence, D., Gasdaska, C., Demmons, N., McCormick, R., Falkos, P., Young, J., and Connolly, W., "Colloid thrusters for the new millennium, ST7 DRS mission," *2004 IEEE Aerospace Conference Proceedings (IEEE Cat. No.04TH8720)*, 2004. https://doi.org/10.1109/AERO.2004.1367606.

[33] Hansel, G. J., "Power conversion and scaling for vanishingly small satellites with electric propulsion," Master's thesis, Massachusetts Institute of Technology, 2014.

[34] Visee, R., de Jong, M., and Timmerman, J., "Miniaturized HV power supply," *Proc. 33rd Int. Electric Propulsion Conf.(Washington, Oct. 2013)*, 2013, pp. 1–8.

[35] Stelwagen, I., De Jong, M., Xu, W., Visee, R., Grustan-Gutierrez, E., Redwood, O., Huh, J., Gray, H., Giannetti, V., Liljeholm, L., GrÃ¶nland, T.-A., and Stark, J., "Development of a high-performance low-cost PPU for an electrospray colloid electric propulsion system for small satellite applications," 2018. URL https://www.scopus.com/inward/record.uri?eid=2-s2.0-85065288500&partnerID=40&md5=5d8f5f03ce705e79c81ab4c6510df2f2.

[36] Baddipadiga, B. P. R., Prabhala, V. A. K., and Ferdowsi, M., "A Family of High-Voltage-Gain DC–DC Converters Based on a Generalized Structure," *IEEE Transactions on Power Electronics*, Vol. 33, No. 10, 2018, pp. 8399–8411. https://doi.org/10.1109/TPEL.2017.2777451.

[37] Weston, S., Miller, C. S., Ingersoll, J. E., Yost, B. D., Agasid, E., Burton, R., Carlino, R., Defouw, G., Perez, A. D., Karacalioglu, A. G., Klamm, B., Rademacher, A., Schalkwyck, J., Shimmin, R., and Tilles, J., "State Of The Art: Small Spacecraft Technology," Tech. rep., National Aeronautics and Space Administration, 2018.

[38] Chin, K. B., Brandon, E. J., Bugga, R. V., Smart, M. C., Jones, S. C., Krause, F. C., West, W. C., and Bolotin, G. G., "Energy Storage Technologies for Small Satellite Applications," *Proceedings of the IEEE*, Vol. 106, No. 3, 2018, pp. 419–428. https://doi.org/10.1109/JPROC.2018.2793158.

[39] Krause, F. C., Loveland, J. A., Smart, M. C., Brandon, E. J., and Bugga, R. V., "Implementation of commercial Li-ion cells on the MarCO deep space CubeSats," *Journal of Power Sources*, Vol. 449, 2020, p. 227544. https://doi.org/https://doi.org/10.1016/j.jpowsour.2019.227544.

[40] Nieto-Peroy, C., and Emami, M. R., "CubeSat Mission: From Design to Operation," *Applied Sciences*, Vol. 9, No. 15, 2019. https://doi.org/10.3390/app9153110.

[41] Veeramraju, K. J., Eisen, J., Rovey, J. L., and Kimball, J. W., "A New Discontinuous Conduction Mode in a Transformer Coupled High Gain DC-DC Converter," *2022 IEEE Applied Power Electronics Conference and Exposition (APEC)*, 2022, pp. 237–244. https://doi.org/10.1109/APEC43599.2022.9773417.

[42] Erickson, R. W., and Maksimovic, D., *Fundamentals of Power Electronics*, Springer Science & Business Media, 2007.

[43] Matei, C., Urbonas, J., Votsi, H., Kendig, D., and Aaen, P. H., "Dynamic Temperature Measurements of a GaN DC–DC Boost Converter at MHz Frequencies," *IEEE Transactions on Power Electronics*, Vol. 35, No. 8, 2020, pp. 8303–8310. https://doi.org/10.1109/TPEL.2020.2964996.

[44] Ahmed, O., Khan, Y., Butt, M. A., Kazanskiy, N. L., and Khonina, S. N., "Performance Comparison of Silicon- and Gallium-Nitride-Based MOSFETs for a Power-Efficient, DC-to-DC Flyback Converter," *Electronics*, Vol. 11, No. 8, 2022. https://doi.org/10.3390/electronics11081222, URL https://www.mdpi.com/2079-9292/11/8/1222.

[45] Deng, L., Wang, P., Li, X., Xiao, H., and Peng, T., "Investigation on the Parasitic Capacitance of High Frequency and High Voltage Transformers of Multi-Section Windings," *IEEE Access*, Vol. 8, 2020, pp. 14065–14073. https://doi.org/10.1109/ACCESS.2020.2966496.

[46] Sharma, A., and Kimball, J. W., "Novel Transformer with Variable Leakage and Magnetizing Inductances," *2021 IEEE Energy Conversion Congress and Exposition (ECCE)*, 2021, pp. 2155–2161. https://doi.org/10.1109/ECCE47101.2021.9595797.

[47] McLyman, C. W. T., *Transformer and Inductor Design Handbook*, 4$^{\text{th}}$ ed., CRC Press, 2016.

[48] Dalessandro, L., da Silveira Cavalcante, F., and Kolar, J. W., "Self-Capacitance of High-Voltage Transformers," *IEEE Transactions on Power Electronics*, Vol. 22, No. 5, 2007, pp. 2081–2092. https://doi.org/10.1109/TPEL.2007.904252.

[49] Krejci, D., Mier-Hicks, F., Fucetola, C., Lozano, P., Hsu, A., and Martel, F., "Design and Characterization of a Scalable ion Electrospray Propulsion System," 2015.

[50] Williams, T., and Thomas, J., "A Comparison of the Noise and Voltage Coefficients of Precision Metal Film and Carbon Film Resistors," *IRE Transactions on Component Parts*, Vol. 6, No. 2, 1959, pp. 58–62. https://doi.org/10.1109/TCP.1959.1136280.

[51] Miyaoka, Y., and Kurosawa, M., "Measurement of current noise and distortion in resistors," *Proceedings of the International Congress on Acoustics*, Vol. 2019-September, 2019, pp. 3120–3125. https://doi.org/10.18154/RWTH-CONV-239814.